Photochemistry and Photobiology, 2022, 98: 736–747

Special Issue Research Article

Quantifying the Photochemical Damage Potential of Contrast-Enhanced Fluorescence Imaging Products: Singlet Oxygen Production†

Brandon Gaitan[1], Lucas Frankle[1], Shruti Vig[1], Ellen Oskoui[2], Miriam Adwan[1], Yu Chen[3], Rosalie Elespuru[2], Huang-Chiao Huang[1,*,‡] and T. Joshua Pfefer[2‡]

[1]Fischell Department of Bioengineering, University of Maryland, College Park, MD
[2]Food and Drug Administration, Center for Devices and Radiological Health, Silver Spring, MD
[3]Department of Biomedical Engineering, University of Massachusetts-Amherst, Amherst, MA

Received 29 December 2021, revised 17 March 2022, accepted 11 April 2022, DOI: 10.1111/php.13638

ABSTRACT

The benefits of contrast-enhancing imaging probes have become apparent over the past decade. However, there is a gap in the literature when it comes to the assessment of the phototoxic potential of imaging probes and systems emitting visible and/or near-infrared radiation. The primary mechanism of fluorescent agent phototoxicity is thought to involve the production of reactive molecular species (RMS), yet little has been published on the best practices for safety evaluation of RMS production levels for clinical products. We have proposed methods involving a cell-free assay to quantify singlet oxygen [(SO) a known RMS] generation of imaging probes, and performed testing of Indocyanine Green (ICG), Proflavine, Methylene Blue, IR700 and IR800 at clinically relevant concentrations and radiant exposures. Results indicated that SO production from IR800 and ICG were more than two orders of magnitude below that of the known SO generator Rose Bengal. Methylene Blue and IR700 produced much higher SO levels than ICG and IR800. These results were in good agreement with data from the literature. While agents that exhibit spectral overlap with the assay may be more prone to errors, our tests for one of these agents (Proflavine) appeared robust. Overall, our results indicate that this methodology shows promise for assessing the phototoxic potential of fluorophores due to SO production.

INTRODUCTION

Recent advances in optical imaging have the potential to significantly improve patient outcomes, with one of the most promising intraoperative approaches being contrast-enhanced fluorescence imaging. This technique has the advantage of being real-time, minimally invasive and increasingly accepted by clinicians. The three primary types of contrast-enhanced fluorescence imaging procedures include those involving: nontargeted dyes, metabolically localizing fluorophores and molecular-targeted agents.

Over the past 20 years, two of the most widely used clinical fluorophores have been Indocyanine Green (ICG) and fluorescein. These agents have found success as nontargeted dyes, particularly for use in procedures such as retinal angiography (1,2) and fluorescence-guided surgical resection (3,4). Methylene Blue is another nontargeted fluorophore, initially being not only found to selectively stain cells with dysplasia in Barrett's esophagus (5), but also studied as a cancer imaging agent (6,7).

Due to the clinical effectiveness of untargeted fluorophores, researchers began to develop fluorophores capable of localizing in dysplastic cells. One agent that has been studied clinically is Proflavine, particularly for its ability to image cancerous tissue, including oral carcinomas (8). Metabolic imaging agents, with one of the most prominent examples being 5-aminolevulinic acid (5-ALA)–induced protoporphyrin IX (PpIX), tend to selectively accumulate in tumors (9,10). This accumulation has been leveraged to aid in the resection of glioblastoma during fluorescence-guided surgery, with PpIX specifically allowing the surgeon to better visualize tumors compared with white light imaging (11,12).

More recently, molecular-targeted imaging agents have begun to achieve clinical viability. Antibody-labeled probes have been developed to target tumor tissue to aid in surgical guidance. These fluorophores are conjugated to tumor-targeting compounds to select specific cell surface proteins to bind to, allowing for localized and targeted imaging (13). One example is a folate-receptor-α-targeted probe used to aid in the removal of cervical cancer (14). Often, fluorescence molecular imaging agents employ newer probes that emit fluorescence in the near-infrared (NIR) "optical window" wavelength range, which should enable higher contrast and deeper penetration imaging. One example is IR800, which is normally used as a targeted imaging agent through conjugation to a monoclonal antibody, being used in over 15 clinical trials. Many of these trials are for the fluorescence-guided surgery of different types of cancer, such as glioblastoma (NCT03510208), esophageal carcinomas (NCT03558724) and breast cancer (NCT02583568).

*Corresponding author email: hchuang@umd.edu (Huang-Chiao Huang)
†This article is part of a Special Issue dedicated to the topic of Emerging Developments in Photocaging.
‡These authors contributed equally to this work.

IR700 was initially used to image colorectal cancer (15,16) and pancreatic cancer (17) in mice. Another set of dyes that have gained popularity for targeted imaging are "Cy" series dyes (Lumiprobe, Hunt Valley, MD) which fluoresce in the red to NIR spectral range, and can be conjugated to antibodies to aid in the imaging of different cancers (18,19).

When exposed to light at certain wavelengths, fluorophores can exhibit photochemical processes that produce phototoxicity (20). These processes are similar to photochemical effects of tissue exposure to ultraviolet radiation which can cause DNA damage—a scenario that is addressed in existing optical radiation safety standards such as in the IEC 60825–1:2017. The primary mechanism of phototoxicity involves the production of reactive molecular species (RMS) such as singlet oxygen (SO), superoxide anions, hydrogen peroxide and hydroxyl radicals (21,22). RMS can cause damage to cells directly through protein oxidation, which can inhibit certain enzymatic processes (23), lipid peroxidation, that can cause damage to cellular membranes (24), and nucleic oxidation, which can cause DNA damage and lead to necrosis and/or apoptosis (25). The production of RMS involves the absorption of light that excites the electrons from the ground state to its excited singlet state. When the electron relaxes back down to the ground state, light can be emitted in the form of fluorescence, but another possibility is that after excitation, the electrons go to a triplet state that allows for the transfer of energy to ground state molecules, creating RMS. Perhaps, the most significant RMS is SO. In addition to being the most well-studied form of RMS, SO is a commonly generated species since it represents oxygen's lowest excited state (26,27). Additionally, SO has one of the largest redox potentials when compared to other RMS, with a reduction potential of 0.92 E_0/V (27); thus, it is more likely to react with its surrounding environment. While prior studies have focused on developing test methods for the detection of phototoxicity and SO (28,29), none have focused on quantifying the potential toxicity of fluorescent imaging products using test methods that might be widely adopted.

Because the process of RMS production and fluorescence are closely related, several agents appear to be capable of dual use, in either imaging or phototherapy. For example, PpIX is used in fluorescence-guided resection, but its phototoxic effects have also been leveraged as a cancer treatment agent when administered at a higher irradiance and longer exposure time (30,31). Another is IR700, which has not only been used as an imaging agent but has also been found to produce high levels of RMS. This feature has been exploited to treat bladder (32), lung (33) and breast (34) cancer using photodynamic therapy (PDT), acting as a targeted treatment agent through conjugation to an antibody. Methylene Blue is another agent that has not only found off-label use as an imaging agent but has also been found to produce RMS, leading to DNA damage *in vivo* (35,36). Proflavine has not only been investigated as an imaging agent to detect oral carcinomas (8) but has also been used as a PDT agent to inactivate the herpes simplex virus (37). Therefore, it is important to go beyond identifying fluorophores as phototoxic or nonphototoxic, rather, to evaluate each imaging product as a whole—the agent, device and dosing regime together—to ensure patient safety while not adversely impacting innovation.

A variety of methods have been implemented to evaluate phototoxicity, including cytotoxicity assays (3 T3-NRU), and markers of DNA damage such as the comet assay (38). Guidance documents provided by the Center for Drug Evaluation and Research (CDER) and Center for Biologics Evaluation and Research (CBER) provide recommendations to perform RMS testing. Although RMS testing methods have been defined, these methodologies have fixed concentrations, radiant exposures (H_e) and wavelengths regardless of the fluorescent probes' clinical use parameters, focusing more on phototoxicity caused by sunlight. For example, OECD/OCDE TG 432 guidelines call for the use of a solar simulator, emitting wavelengths between 290 nm-700 nm and a H_e of 5 J cm^{-2}. The International Council for Harmonisation of Technical Requirements for Pharmaceuticals for Human Use (ICH) also points out the need to perform initial *in vitro* phototoxicity tests before clinical trials are performed. Although the importance of determining the potential phototoxicity of drugs has been established, no literature has been published developing or evaluating a testing methodology that focuses on phototoxicity screening of products intended for imaging, which may involve dual-use fluorophores at biologically safe levels.

The purpose of this research is to facilitate the development and clinical translation of emerging contrast-enhanced fluorescence imaging products through the establishment of a standardized and least burdensome methodology for phototoxicity screening. This aligns with safety evaluation needs described in a 2017 Consensus Meeting Report by authors from academia, industry and government agencies (39). Through the use of a battery of cell-free assays, it may be possible to screen imaging products for the potential to produce substantial RMS, and thus the need for further testing (*e.g.* cell-based assays). In this study, our primary goal was to evaluate an approach based on a commercial assay to quantify SO production in an objective, quantitative and consistent manner. This involved performing measurements that elucidate differences between well-known fluorophores under a range of clinically relevant dosing scenarios. In addition to providing insights into RMS generation in specific agents and the limitations of the assay approach, this report describes potential best practices for standardizing preclinical phototoxicity screening of contrast-enhanced fluorescence imaging products.

MATERIALS AND METHODS

Overview. This study involved three main phases: (1) determination of relevant agent concentrations, optical exposure wavelengths and radiant exposure levels through an extensive literature search of clinical and animal studies; (2) exposure of each agent over a range of concentrations and radiant exposures and measurement of fluorescence levels generated by a commercial SO assay for each case; and (3) analysis of the results to assess agreement with the literature, differences and similarities between agents, and overall performance and limitations of the assay. Through these steps, our intent was to evaluate the potential of this approach, identify best practices for its standardized implementation and provide insight into the SO generation potential of specific agents.

SO assay. The assay used to detect SO produced by the fluorophore is a commercially available product, Singlet Oxygen Sensor Green ([SOSG] Thermo Fisher, Eugene, OR) that has been used in numerous prior studies (28,40–42). SOSG has been used for over a decade, becoming one of the most widely used methods for measuring SO due to its high specificity, being activated minimally by other RMS such as hydrogen peroxide and superoxides (43). SOSG is used regularly to qualify the amount of SO produced by phototoxic molecules in the field of PDT (42,44). SOSG is likely composed of a fluorescein-based dyad that is bonded to an anthracene moiety. In its normal state, the anthracene quenches the fluorescein, inhibiting its fluorescence. When exposed to SO, the anthracene gets converted to endoperoxide, which does not cause intermolecular quenching, allowing the fluorescein to fluoresce (40,45).

The SOSG assay was prepared by mixing a single 100 μg vial with 330 μL of methanol to make a final concentration of 500 μM. The solution was diluted with deionized (DI) water to a SOSG concentration of 7 μM in the well plate and mixed with the individual fluorophore solutions described below. The SOSG assay was found to have an absorption peak at 485 nm and an emission peak at 522 nm, as seen in Fig. 3.

Fluorophore concentrations and illumination levels. The rate of RMS generation depends on the spectrum and H_e of the light source, as well as the concentration of the fluorescent agent. Therefore, we attempted to replicate clinically relevant scenarios—illumination wavelengths and maximum H_e′s were determined from clinical studies and *in vivo* experiments for individual fluorophores. Illumination was performed from a very low level to approximately twice the likely maximum clinical H_e. After a fluorophore concentration was identified as the most clinically relevant level, a set of values from near zero to approximately twice the maximum clinically relevant level were used to evaluate variations in SO production.

A limited review of literature enabled the identification of appropriate parameter spaces for the exposure of each agent. ICG (Adooq® BioScience, Irvine, CA) was reconstituted in DI water and diluted to a stock concentration of 1 mM and stored at 0°C while wrapped in foil to avoid light exposure. The concentration range used was 6.5–26 μM, and the H_e range was 0–20 J cm^{-2} and excited at a wavelength of 785 nm. ICG doses were based on blood plasma values found in human subjects (46,47). The H_e and wavelength of 785 nm were derived from values used for fluorescent-guided surgery (48). A concentration range of 1–7.5 μM for Methylene Blue (Sigma Aldrich, St. Louis, MO) was used, based on pharmacokinetics data acquired after intravenous administration of 100 mg in human subjects (49). The H_e of 0–6 J cm^{-2} was determined through camera exposure times required during open surgery (50). The concentration range used for IR800 (LI-COR, Inc, Lincoln, NE) was between 2.5 and 20 μM, determined based on clinical studies using IR800 as a contrast agent for fluorescence-guided surgery (51,52). The IR700 (Li-COR, Lincoln, NE) concentration range of 0.125–1 μM was based on *in vivo* studies where blood and the serum concentration were measured in rodents (53), as well as the biodistribution of IR700 measured in macaques (54). For both IR700 and IR800, the H_e range was 0–6 J cm^{-2}, based on current imaging devices and the likely duration of imaging during surgery (55), with the wavelengths of 785 and 685 nm also taken from the excitation wavelengths of currently used devices (55). For proflavine (Sigma Aldrich), we used a concentration range of 1.5–12 μM, a H_e range of 0–6 J cm^{-2}, and excited at 445 nm. The concentrations, H_e′s and wavelength used, were based on human trials using proflavine as an imaging agent to detect oral cancer (8,56). Rose Bengal (Sigma Aldrich) is not a clinical imaging agent but was included as a positive control since it is known to generate large amounts of SO, to the point where it has been used as a light-activated anti-microbial agent (57). Rose Bengal concentrations (0.5–4 μM), exposure levels (H_e of 0–1 J cm^{-2}) and wavelength were selected to achieve similar clinical exposure levels as the other fluorophores tested, to directly compare results. For all fluorophores, 165 μL of the dilution was placed into individual wells in a 96-well plate. A brief literature review of *in vivo* concentrations and illumination parameters for each fluorophore is provided in Table 1. The concentrations, excitations wavelengths, irradiances and H_e′s used in the experiment are summarized in Table 2.

Optical exposure and measurement approaches. A custom setup was developed to illuminate samples in a 96-well plate (Fig. 1). The system is composed of a laser diode controller (Thorlabs, Inc, Newton, NJ), a laser diode, a collimator ($f = 50$ mm) and a 20° square diffuser (ED1-S50-MD, Thorlabs, Inc.). The system was set to illuminate a 7 cm × 7 cm area, but only a 2.5 cm × 1.75 cm area (six wells in a 96-well plate) was used, choosing a six-well area with a variation [(max irradiance-min irradiance)/max irradiance] of <10%. The two main reasons that a max variation of 10% was chosen is that this is approaching the limits of our setup due to certain nonuniformities in our laser diodes, and at this max variance, the conclusions drawn in this study would not be impacted. Ideally, the variance would be reduced in the future through the use of more uniform laser diodes. TO-can lasers (Thorlabs, Inc.) were used to expose the different fluorophores, with the following central wavelengths: 520 nm (Rose Bengal), 785 nm (ICG/IR800), 660 nm (Methylene Blue), 685 nm (IR700) and 450 nm (Proflavine). These are the wavelengths most commonly used to excite each fluorophore in a clinical setting. After each plate of samples was illuminated for the appropriate duration to achieve the desired total H_e, assay fluorescence was measured using a plate reader (Synergy Neo2, BioTek, Winooski, VT) with an excitation wavelength of 485/18 nm and an emission wavelength of 535/26 nm to enable measurement of assay fluorescence, with the plate reader delivering maximum energy of 25 mJ cm^{-2} per reading for the excitation.

Phototoxicity assay procedure. Before proceeding to measurement trials, the concentration of the dilutions was all tested for accuracy using an absorbance measurement, where concentration was calculated using known molar extinction coefficients. Samples were either accepted or remade to correct any errors. The laser system was set to the appropriate irradiance level (Table 2) and verified using a power meter (model PMD100D, Thorlabs, Inc.). A volume of 165 μL of the fluorophore of interest at 2× the desired concentration was mixed with 165 μL of 14 μM SOSG dissolved in DI water in a 96-well plate, resulting in a mixture of 7 μM of SOSG and the exact desired concentration of the fluorophore of interest. This mixture was prepared with 5–6 replicates depending on the amount of evenly distributed light that can be exposed onto the plate for each given laser and its required irradiance. Three wells were filled with the fluorophore and assay mixture, but these would be covered to avoid exposure to the laser and serve as a dark, negative control. Three more wells were filled with DI water to serve as a blank. These were all placed on the edges of the plate and covered with foil. Controls included three wells that are one-part DI water and one-part fluorophore of interest, measured at the same excitation and emission wavelengths as SOSG. This control aided in the quantification of the cross-talk between the SOSG probe measurement and the fluorophore of interest, with the results in Fig. 6c. The 96-well plate was initially read with no laser excitation. After the initial reading, the 96-well plate was illuminated to achieve the desired H_e, then it was again measured by the plate reader. When the plate was not being illuminated or measured, it was shielded from any ambient light. This process was repeated at predetermined intervals until the maximum H_e was reached. To assess repeatability, every concentration of each fluorophore was repeated four to six times. A diagram of the process is shown in Fig. 2.

Data analysis. Fluorescence signals collected for a given concentration of a fluorophore were normalized to using the formula below:

$$\text{Normalized FL}_{\text{SOSG}} = \frac{\left(\text{FL}_{\text{SOSG+Fluo.(Exp):H}_e} - \text{FL}_{\text{SOSG+Fluo.(DarkControl):H}_e}\right) - \left(\text{FL}_{\text{SOSG+Fluo.(Exp):0}_J} - \text{FL}_{\text{SOSG+Fluo.(DarkControl):0}_J}\right)}{\text{FL}_{\text{SOSG}}} \quad (1)$$

where $\text{FL}_{\text{SOSG + Fluo.(Exp):He}}$ is the fluorescence intensity of the SOSG probe and fluorophore at the specific H_e, $\text{FL}_{\text{SOSG + Fluo.(Dark Control):He}}$ is the corresponding dark control at the same H_e equivalent time (since they are not exposed to excitation light), $\text{FL}_{\text{SOSG + Fluo.(Exp):0J}}$ and $\text{FL}_{\text{SOSG + Fluo.(Dark Control):0J}}$ are the experimental and control fluorescence at 0 J cm^{-2} and FL_{SOSG} is the average fluorescence intensity of SOSG alone. The mean and standard deviation were calculated and graphed as a function of H_e. This was repeated for each fluorophore concentration. The results from the repetitions were averaged to generate a final plot with variance represented by error bars. The slope of each of these lines was found using linear regression and setting the *y*-intercept to 0. When performing the linear regression, the R^2 value should be >0.96 if the peak-normalized fluorescence value for the highest concentration is above 1. If the R^2 values are below 0.96, the highest H_e value should be dropped and the R^2 recalculated. If the peak-normalized fluorescence value is below 1, then the R^2 value threshold can be dropped to 0.93 due to a loss of sensitivity of the assay at lower fluorescence values. We then plotted the calculated slope against the concentration, giving the SO production rate. This allowed all fluorophores to be viewed together in one figure (Fig. 5). The SO production factor is then derived by taking the slope of the SO production rate *vs* concentration. The three wells that served as negative controls were also plotted in the same manner as the experimental data and then subtracted from the experimental data.

All data were plotted and analyzed using the graphing software PRISM (San Diego, CA) and was plotted using standard error mean.

RESULTS

Figure 3 shows the normalized absorption and emission spectra of the assay and other fluorophores used in this study. SOSG assay absorption and emission peaks are seen at 490 and 530 nm, respectively. For most of the fluorophores tested, there

Table 1. Literature review summary focusing on the clinical use of imaging fluorophores: concentration, excitation wavelength and irradiance.

Fluorophore	Model	Use case	Conc.	Excitation wavelength	Irradiance	Imaging time	Citation
ICG	Human	Lymphatic imaging	0.2 mL Injected	760 nm	NA	NA	Unno, N. *et al*, 2007 (69)
	Human	Lymphatic imaging	1 mL of 0.5% ICG Injected	750–800 nm	NA	30 min	Takeuchi, M. *et al*, 2012 (75)
	Human	Blood conc. of ICG	5–30 mg L^{-1} in plasma	805 nm	NA	NA	Imai, T., 1998 (76)
	NA	Instrument review	NA	785 nm	1.9 mW cm^{-2}	NA	Zhu, B., 2015 (48)
	Human	lymph node imaging	1 mL Injected	760 nm	4 mW cm^{-2}	15 min	Tagaya, T., 2008 (77)
IR800	Human	Head and neck surgery	5.2–130 mg total injected	775 nm	NA	NA	Gao, R., *et al*, 2018 (51)
	Human	Glioblastoma imaging	50–100 mg injected	NA	NA	NA	Miller, S., *et al*, 2018 (52)
	NA	Instrument review	NA	780 nm	3–30 mW cm^{-2}	NA	D'Souza, A., *et al*, 2016 (55)
Proflavine	Human	Oral cancer imaging	0.01% (w/v)	455 nm	NA	NA	Shin, D., *et al*, 2010 (8)
	Human	Oral cancer imaging	0.01%	455 nm	NA	3–15 min	NCT01269190 (2016)
	Human	Imaging of Barrett's-Related Neoplasia	0.01% (w/v)	435/500 nm	8.2 mW/14.9 mW	NA	Tang, Y., *et al*, 2016 (56)
Methylene Blue	Human	Intravenous bioavailability	600–2000 ng mL^{-1} in blood	NA	NA	NA	Stefano, A., *et al*, 2018 (78)
	Swine	Uterine imaging	0.1 mg kg^{-1} Injected	670 nm	2.5 mW cm^{-2}	NA	Matsui, A., *et al*, 2010 (50)
	Human	Uterine imaging	0.25–1 mg kg^{-1} injected	670 nm	1.08 mW cm^{-2}	>5 min	Verbeek, F., *et al*, 2013 (6)
	Human	Breast cancer imaging	1 mg kg^{-1} injected	670 nm	1.08 mW cm^{-2}	NA	Tummers, Q., *et al*, 2014 (7)
IR700	Primate	Biodistribution of Injected	0.1–10 μg g^{-1} present in tissue	700 nm	NA	NA	Boer, E., *et al*, 2015 (54)
	Mouse	EGFR Targeting	100 μg injected	689 nm	25 mW	2–20 min	Sato, K., *et al*, 2014 (79)
	NA	Instrument Review	NA	680 nm	3–30 mW cm^{-2}	NA	D'Souza, A., *et al*, 2016 (55)

is minimal crossover in excitation and emission with the assay. The exception to this is Proflavine, which has considerable overlap with the assay in both excitation and emission wavelengths.

In Fig. 4, we present assay fluorescence as a function of H_e for all the fluorophores used in this study. For products incorporating two of the imaging agents, IR800 and ICG, modest increases in assay fluorescence with H_e are apparent, yet the maximum normalized fluorescence level was very low, in the 0.2–0.6 range. These agents also demonstrate minimal correlation with concentration. For example, although ICG and IR800 assay fluorescence does increase with H_e, there is no difference in fluorescence across concentrations. Proflavine also shows an increase in fluorescence with H_e, yet a monotonic decrease in fluorescence with concentration is also shown. The remaining three fluorophores—Rose Bengal, Methylene Blue and IR700—produced a strong fluorescent signal, indicating strong production of SO. The fluorescence increase with respect to H_e is linear, demonstrating a linear relationship between the level of H_e and SO production. In addition, the slope increases in a linear manner with concentration (further explored in Fig. 5). While the maximum normalized fluorescence produced for these cases ranged from 3 to 11, several of the lower concentration/exposure scenarios produced values <1.

A graphical summary of results from all fluorophores tested is shown in Fig. 5. These results demonstrate the dependence of SO production on the type and concentration of fluorophore, as well as H_e. Because the values in Fig. 5 are taken from the slopes of the plots generated in Fig. 4, the units in Fig. 5 are in units of fluorescence divided by H_e, which we will refer to as the SO production rate. Due to the normalized fluorescence being unitless, the SO production rate has units of $cm^2\ J^{-1}$. The products tested fell into two groups based on their SO production levels. Higher SO generation products included those using Rose Bengal, Methylene Blue and IR700 while products that exhibited relatively low-SO production rates were ICG, IR800 and Proflavine. In Table 3, we present SO production factors, determined from the slopes of the SO production rates in Fig. 4. The result was compared with previously determined values of SO quantum yield from the literature. SO quantum yield is defined as the amount of SO produced per photon absorbed, so the value is always between 0 and 1 (58,59). In Table 3, green shading indicates fluorophores with low-SO production factors and SO quantum yields, while red shading indicates fluorophores with relatively large SO production and quantum yields. Yellow indicates inconclusive results, for reasons that will be addressed in the discussion section. It is also worth noting that a potential discrepancy between the SO production factors and SO quantum yield exists.

Most of the agents demonstrated a linear trend in F/H_e *vs* concentration. However, as shown in the SO production plots for (1) Methylene Blue and (2) Proflavine (Fig. 6), Methylene Blue demonstrated a linear response up to 4 μM, after which the rate plateaued and started to decrease. Proflavine results were unique due to the monotonically decreasing SO production rate found. In addition to having a nonlinear response, proflavine also demonstrated a large amount of cross-talk with the SOSG excitation and emission wavelengths, especially when compared to all the other fluorophores that were measured during this study as seen in Fig. 6c.

DISCUSSION

In this study, the main goal was to assess the potential for developing an effective and reliable approach to quantify the SO

Table 2. Concentration range, excitation wavelength, irradiance and H_e values used in our experiments to generate SOSG production plots.

Fluorophore	Conc. range (μM)	Excitation wavelength (nm)	Irradiance (mW cm^{-2})	Max H_e (J cm^{-2})
ICG	6.5–26	785	3.8	20
IR800	2.5–20	785	5	6
Proflavine	0.5–12	445	2.8	6
MB	1–7.5	665	3.4	6
IR700	0.125–1	685	3.2	6
Rose Bengal	0.5–4	520	1	1

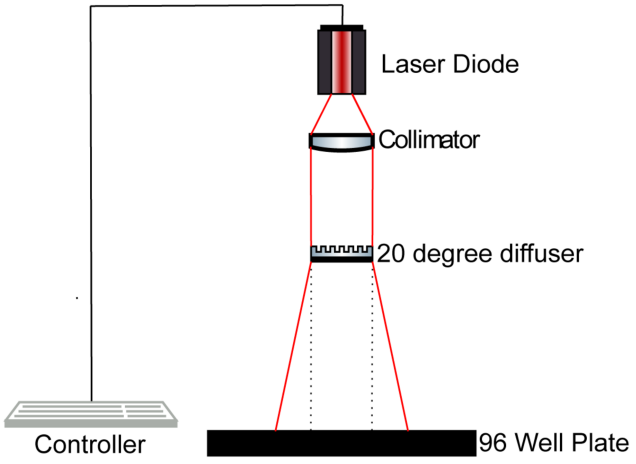

Figure 1. Schematic of the optical exposure system. A laser diode is collimated with a $f = 50$ mm convex lens. The collimated beam passed through a diffuser to create a top-hat beam profile and thus provide uniform irradiance across the 96-well plate.

produced by contrast-enhanced fluorescence imaging products based on an established commercial assay. Our method was able to quantify the amount of SO produced by fluorophores at a specific concentration and excitation wavelength relevant to expected clinical scenarios, which produces important information about the potential phototoxicity of the fluorophore of interest.

Phototoxic potential of tested products

Overall, our results indicate that we can measure and compare the potential SO production of fluorophores at clinical radiant exposure and irradiances. In Fig. 4, results demonstrate that at the highest concentrations and H_e's, ICG and IR800 show peak-normalized assay fluorescence values below 0.6, whereas the positive control Rose Bengal, as well as Methylene Blue and IR700, generated values between 3 and 10 for the highest concentrations and H_e's. The threshold between low and high SO was established based on the highest normalized fluorescence value produced by ICG, a contrast agent with a long history of safe clinical use. Because ICG is not known to cause phototoxic damage at clinically relevant H_e's and concentrations, values below its peak-normalized FL_{SOSG} of 0.6 (seen in Fig. 4a) can be deemed as having low-SO toxicity. Values that fall above this threshold can then be classified as potentially producing SO toxicity. From the data in Fig. 5, we calculated the SO production factor for each agent and compared them to the SO quantum yield values published in the literature (Table 3). Figures 4 and 5 indicated that ICG and IR800 exhibited much lower phototoxic potential than the other three agents. It is worth noting that for agents with higher phototoxic potential, using low H_e and/or concentration combinations could minimize SO generation levels to a point where potentially safe exposures can be performed if the normalized FL_{SOSG} values fall below 0.6. In Fig. 5, while changes in SO production were dose-dependent for these agents, ICG's SO production rate was always under 0.04, and for

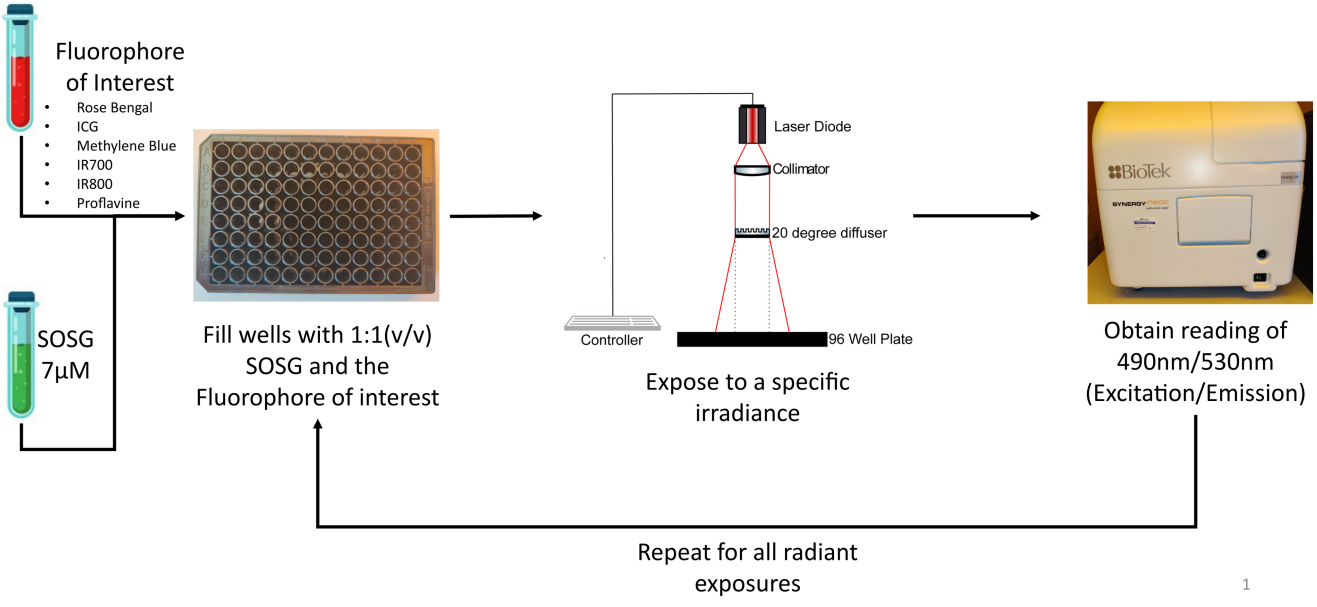

Figure 2. Schematic of procedure used to determine assay fluorescence levels for each sample. The fluorophore of interest (at a specific concentration) and assay were mixed in a well plate, exposed to clinically relevant laser illumination, then measured in a plate reader. Exposures and measurements were then repeated at all designated H_e values and fluorophore concentrations.

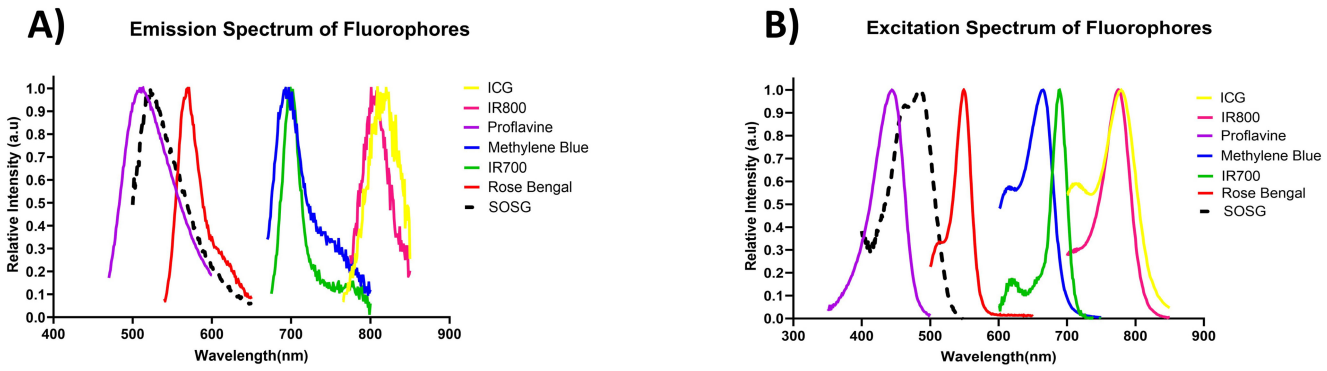

Figure 3. Peak-normalized graphs of (A) excitation and (B) emission wavelengths of the fluorophores used in the study as well as the SOSG probe.

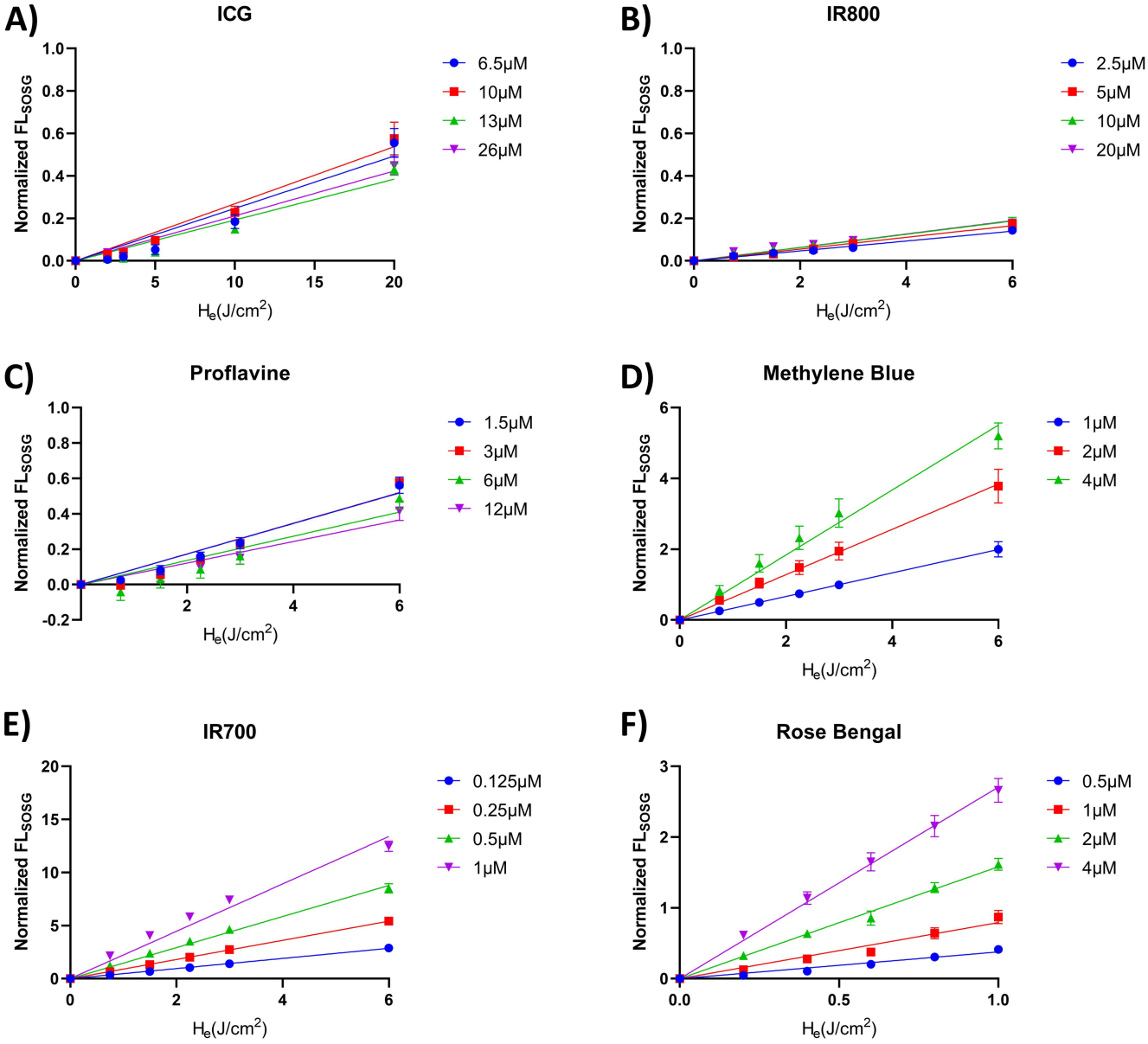

Figure 4. Effect of H_e and fluorophore concentration on SOSG assay fluorescence intensity for (A) ICG, (B) IR800, (C) Proflavine, (D) Methylene Blue, (E) IR700 and (F) Rose Bengal.

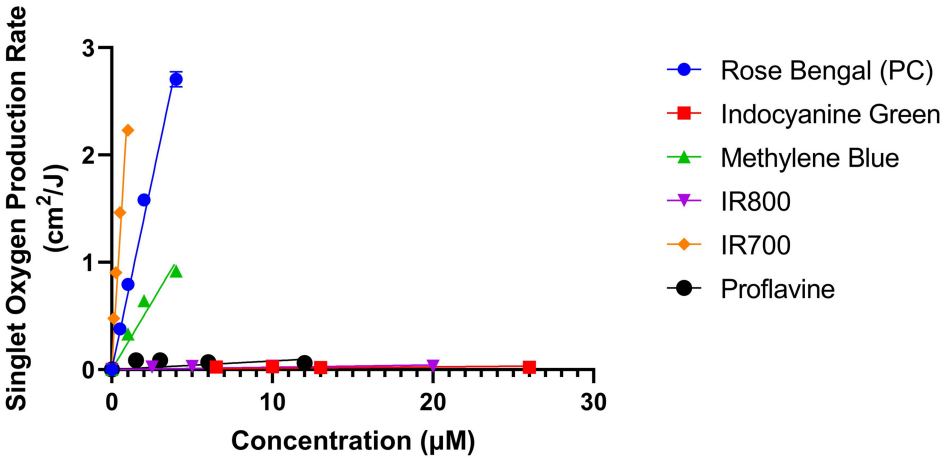

Figure 5. Summary of SO production for all agents tested. SO production rate values represent the mean slopes of the data in Fig. 4 for different fluorophores at their various tested concentrations. Linear regression was performed to obtain SO production factors (Table 3).

IR700, the SO production rate was above 0.4, even at the lowest concentration tested of 0.125 μM. These findings seemed to indicate that increased drug or light doses would not significantly impact the phototoxic potential of products incorporating these agents, although additional study at higher doses would be needed to confirm this behavior.

Additional support for our finding that the tested agents tended to fall into either a high or low-SO-generating category can be found in the literature. The agents which had high-SO production factors have been used as photo-therapeutic agents, including Rose Bengal as a light-activated anti-microbial agent in prior studies (57), and IR700 as a photodynamic agent to treat head and neck cancer (NCT02422979). Methylene Blue is used as a white light contrast agent during gastrointestinal chromoendoscopy procedures, to enhance the detection of neoplastic lesions (60). It has also been used as a fluorescent agent to image the uterus (6), thyroid (61) and pancreas (62). Despite this clinical history, our results and previous literature indicate that Methylene Blue can generate significant quantities of SO, with adverse impacts ranging from patients developing skin rashes (63) to the death of preterm neonates (64,65). In addition, Methylene Blue is likely the source of the DNA damage documented in Barrett's esophagus noted in prior studies (36,66). Although our study did not explicitly address the drug and light doses involved in this study, SO production is likely a factor, which may be of particular concern given the metaplastic/precancerous state of this tissue.

The two agents found to have the lowest SO-generating potential—ICG and IR800—are primarily used as imaging agents. ICG has been extensively used for retinal angiography (67), vascular neurosurgery (68) and more recently for lymphatic imaging (69). Both ICG and IR800 have been used to aid in fluorescent-guided resection (51,70). We are not aware of significant clinical evidence of phototoxicity with either of these agents, with studies demonstrating ICG's efficacy and safety for use in lymph node dissection (71), and clinical trials using IR800 demonstrating no serious adverse side effects in clinical imaging trials (52). Thus, it is likely that the fluorescence assay readings produced during the testing of these agents also represent safe levels. However, it is worth noting that a prior study has indicated that ICG produces SO that rapidly oxidizes the ICG molecule, leading to decomposition and formation of cytotoxic components (72).

The SO production factors are shown in Table 3 are derived from the SO production rates in Fig. 4 by taking the slopes of the concentration *vs* the SO production rate. Because of this, the SO production factor is dependent on concentration and H_e, having the units of cm^2 per J*μM. In addition, the SO production factor is still dependent on several other variables, such as the oxygen level in the surrounding region, and the imaging excitation wavelength. The SO production factor can be thought of as an easy way to compare the SO potential of different fluorophores under their own, independent clinical conditions.

As noted in the results section, our SO production factor data show only a moderate degree of quantitative correlation with published SO quantum yields. One possible reason is that the SO quantum yield is independent of environmental factors since it only takes into account the likelihood of generating SO if the compound has already absorbed a photon. One example would be that Rose Bengal has a larger SO quantum yield than IR700, but the reverse is true when comparing SO production factors. But, by looking at the absorbance fraction of the fluorophore at the wavelength used to excite the fluorophore (520 nm/685 nm for Rose Bengal/IR700 respectively), we can see that the absorption fraction for Rose Bengal was 0.33 and for IR700 the absorbance fraction was 0.93. This difference in absorbance is one key factor that could explain the differences between the SO production factor and SO quantum yield.

Potential method limitations

Since the SOSG assay is based on visible wavelength fluorescence, it is not unexpected that there would be an inherent limitation due to interference from test fluorophores that are active in this range. The assay incorporates a fluorescein-based dyad (20,21) and thus has the same excitation and emission as fluorescein (485 nm/535 nm respectively). In our study, the effect of optical interference is seen in the test for Proflavine. Although Proflavine exhibited substantial cross-talk with the assay when measured with a plate reader (Fig. 6c), our current method takes

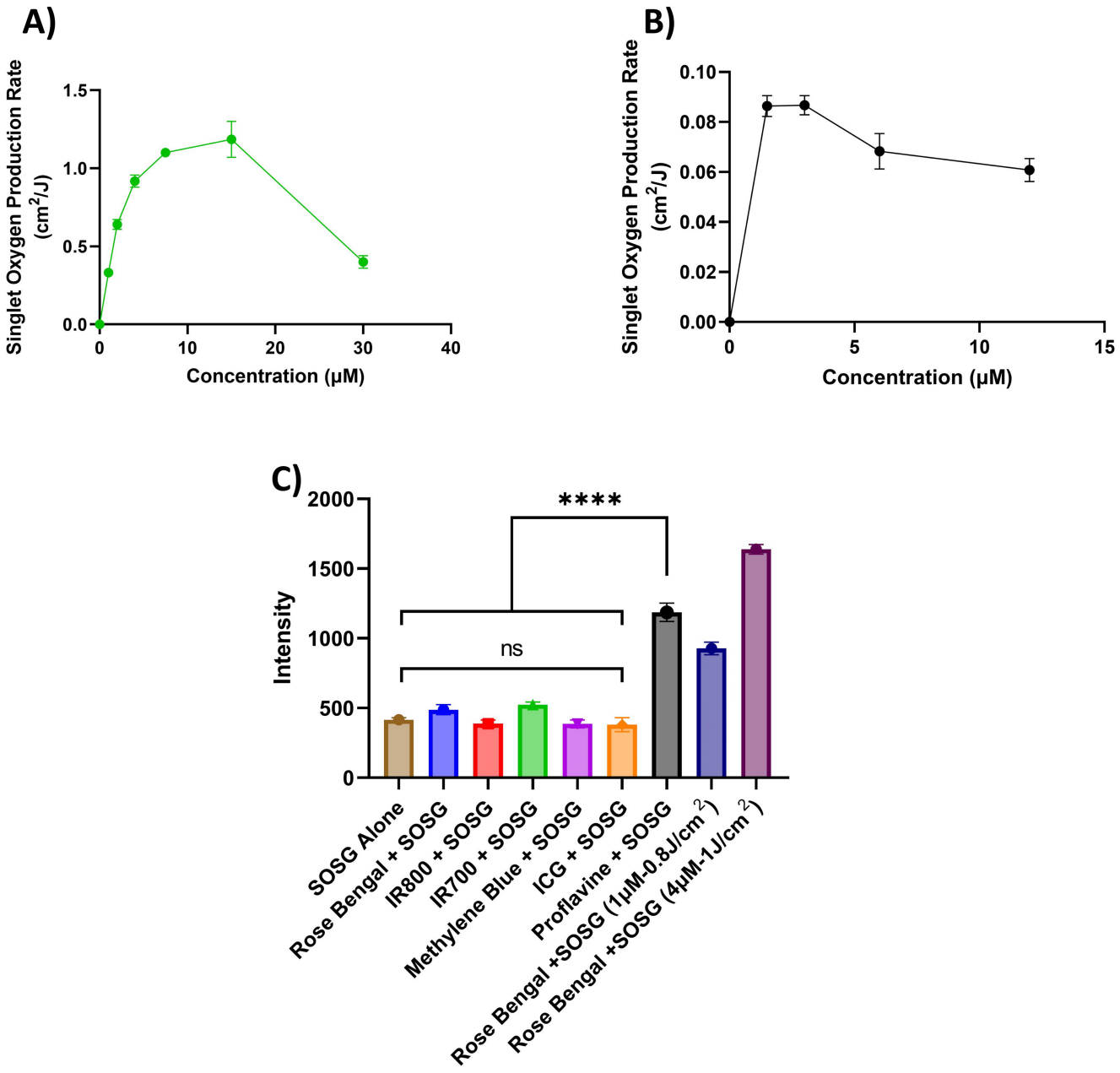

Figure 6. Nonlinear SO production rate plots for (A) Methylene Blue and (B) Proflavine. Figure (C) demonstrates the reading at 0 J for the different fluorophores tested at the excitations/emission of SOSG, the SO signal produced by Rose Bengal and SOSG at the Normalized FL_{SOSG} threshold of 0.6 (concentration of 1 μM, H_e = 0.8 J cm^{-2} for Rose Bengal) and the signal produced by a high-SO generator, in this case, Rose Bengal at a concentration of 4 μM and a H_e of 1 J cm^{-2}.

into account cross-talk effects by implementing a background subtraction using unexposed measurements of fluorophore-only control samples and assay-fluorophore mixtures. By implementing this simple correction approach, we were able to effectively mitigate the presence of Proflavine cross-talk and establish that for the concentrations and radiant exposures used, SO production was low. If Proflavine were to have produced significant SO, the level of increase in assay fluorescence should have been detectable, based on the change in SOSG signal produced by Rose Bengal at higher drug/light doses. However, if higher concentrations of Proflavine were used, or another fluorophore with higher fluorescence yield, the level of cross-talk and variability in detected signals might increase to the point where results would be compromised regardless of the correction approach.

An example of a way to determine whether the cross-talk variance is too large is to compare the variance of the cross-talk value at 0 J cm^{-2} to the fluorescence intensity produced by SOSG at the high/low-SO threshold. This threshold can be seen in Fig. 6c, looking at the fluorescence produced by Rose Bengal and SOSG at a concentration of 1 μM and H_e of 0.8 J cm^{-2} (this is similar to the normalized FL_{SOSG} value of 0.6). If the cross-talk increases the variance to the point that there is no significant

Table 3. Singlet oxygen production factor determined from the slopes in Fig. 5. These results were also compared with literature values of SO quantum yield. Highlighting in this table corresponds to low-SO-producing fluorophores (green), high-SO-producing fluorophores (red) and inconclusive (yellow).

Fluorophore	SO production factor [$(F/H_e)/\mu M$]	SO quantum yield
ICG	0.0012 ± 0.0002	0.077 (**80**)
IR800	0.0021 ± 0.00024	–
Proflavine	0.0080 ± 0.0014	0.12 (**80**)
Rose Bengal	0.70 ± 0.01	0.76 (**80**)
Methylene Blue	0.25 ± 0.01	0.51 (**80**)
IR700	2.44 ± 0.08	0.30 (**81**)

difference between no generation intensity and this threshold value, the cross-talk might be too large to draw conclusive results from the assay. In addition, users should be aware of the potential for shielding if a fluorophore of interest has an overlapping absorbance spectrum with SOSG emission. The test fluorophore could potentially absorb the SOSG signal, leading to erroneously low estimates of SO.

Another unusual result is that of Methylene Blue SO production. After initially increasing linearly with concentration up to 4 μM, assay fluorescence abruptly plateaued, then decreased above 7.5 μM. Unlike the proflavine result, there is little to no interference caused by SOSG and Methylene Blue, as in Fig. 6c we can see that Methylene Blue creates very little cross-talk in the SOSG channel. This means that the issue is likely not the assay itself. A possible reason for the plateau could be specific to Methylene Blue, as studies have shown that it can be converted to the nonfluorescent compound Leucomethylene, due to pH and concentration changes. A study by Matsui *et al.* found that in PBS Methylene Blue fluorescence increases with concentration up to 7.5 μM, then decreases with concentration (50). Since SO production is tied to the mechanism that causes fluorescence, factors that affect Methylene Blue fluorescence can affect SO production.

Implications for phototoxicity evaluation

Our findings provide evidence that when implemented according to a standardized set of best practices, it may be possible to use commercially available assays to screen contrast-enhanced fluorescence imaging devices for photochemical safety. With our methodology, researchers can quickly identify the SO production rate by an imaging probe under expected clinical conditions, using cost-effective materials and equipment available in most laboratories. Benchmarking optical measurements against well-established fluorophores such as Rose Bengal and ICG may also help to optimize consistency in test outputs.

Initially, it is critical to identify the relevant fluorophore concentration range and H_e. The identification of exposure levels that significantly exceed the clinical values can be used to provide a factor of safety. For the fluorophore illumination, source irradiance and exposure duration can typically be adjusted to achieve the appropriate H_e. As long as thermal and multi-photon effects are avoided, photochemical effects are not highly time-dependent (except possibly under conditions of transient environmental conditions). However, it should also be noted that the H_e levels implemented in cell-free assays may need to be greater than clinical exposure levels to account for the true maximum fluence levels that cells would be subject to in turbid biological tissue. As prior studies have shown, subsurface fluence levels can greatly exceed H_e levels, due to tissue scattering/backscattering and resultant isotropic propagation of light (73,74). The cell-free assay approach studied here may obviate the need for cellular and *in vivo* phototoxicity testing in many fluorescence imaging products. However, if initial tests demonstrate a high level of SO generation (a value above 0.6 for the derived normalized SO fluorescence generation), the product would be considered potentially phototoxic, and additional testing is required with more involved methods, such as an *in vitro* photo-cytotoxicity assay. While the current study focuses on the detection of singlet oxygen, a RMS generated through type 2 reactions, other assays will be needed to detect other RMS produced by type 1 reactions, such as hydroxyl radicals and superoxides. These assays will form the basis of a comprehensive test method. By quantifying other key RMSs, a more thorough understanding of a product's phototoxic potential will emerge.

Our future work will focus on two primary needs: (1) cell-free assays to quantify other RMS that can be produced by fluorescent probes and (2) assays to quantify photo-cytotoxicity of agents that have been shown to produce significant RMS. By developing a battery of simple tests to assess phototoxicity, we can provide a least burdensome approach to help ensure patient safety and encourage innovation in fluorophores for a variety of clinical applications.

CONCLUSION

In this study, we have developed and evaluated methods based on a commercial cell-free assay for assessing the potential of fluorophore-device imaging products to generate SO under clinical conditions. Our findings on light/drug dose–response of several well-known fluorophores align well with limited published data available on SO production and phototoxic effects of these agents. While spectral overlap of the assay and fluorophores may impede the effectiveness of this approach, initial results indicate that our method can be largely robust to these challenges under certain conditions. Overall, this study provides evidence of the potential of approaches based on commercial assays as screening methods for fluorescence imaging product phototoxicity.

Acknowledgements—This work is supported by the NSF-FDA scholar-in-residence Program CBET-2037815. Mr. Brandon Gaitan is supported by the Clark Doctoral Fellowship. Mr. Lucas Frankle is supported by the University of Maryland ASPIRE Fellowship. We would also like to acknowledge Anqi He for her contribution in performing background research and aiding in the preliminary experiments.

DISCLAIMER

The mention of commercial products, their sources or their use in connection with material reported herein is not to be construed as either an actual or implied endorsement of such products by the Department of Health and Human Services.

REFERENCES

1. Blauth, C., J. Arnold, E. M. Kohner and K. M. Taylor (1986) Retinal microembolism during cardiopulmonary bypass demonstrated by

fluorescein angiography. *Lancet* **2**(8511), 837–839. https://doi.org/10.1016/s0140-6736(86)92871-0
2. Manivannan, A., J. Plskova, A. Farrow, S. McKay, P. F. Sharp and J. V. Forrester (2005) Ultra-wide-field fluorescein angiography of the ocular fundus. *Am. J. Ophthalmol.* **140**(3), 525–527. https://doi.org/10.1016/j.ajo.2005.02.055
3. Shinoda, J., H. Yano, S.-I. Yoshimura, A. Okumura, Y. Kaku, T. Iwama and N. Sakai (2003) Fluorescence-guided resection of glioblastoma multiforme by using high-dose fluorescein sodium. *J. Neurosurg.* **99**(3), 597–603. https://doi.org/10.3171/jns.2003.99.3.0597
4. Van Der Vorst, J. R., B. E. Schaafsma, M. Hutteman, F. P. R. Verbeek, G.-J. Liefers, H. H. Hartgrink, V. T. H. B. M. Smit, C. W. G. M. Löwik, C. J. H. van de Velde, J. V. Frangioni and A. L. Vahrmeijer (2013) Near-infrared fluorescence-guided resection of colorectal liver metastases. *Cancer* **119**(18), 3411–3418. https://doi.org/10.1002/cncr.28203
5. Canto, M. I. F., S. Setrakian, R. E. Petras, E. Blades, A. Chak and M. V. Sivak (1996) Methylene blue selectively stains intestinal metaplasia in Barrett's esophagus. *Gastrointest. Endosc.* **44**(1), 1–7. https://doi.org/10.1016/S0016-5107(96)70221-3
6. Verbeek, F. P. R., J. R. van der Vorst, B. E. Schaafsma, R.-J. Swijnenburg, K. N. Gaarenstroom, H. W. Elzevier, C. J. H. van de Velde, J. V. Frangioni and A. L. Vahrmeijer (2013) Intraoperative near infrared fluorescence guided identification of the ureters using low dose methylene blue: A first in human experience. *J. Urol.* **190**(2), 574–579. https://doi.org/10.1016/j.juro.2013.02.3187
7. Tummers, Q. R. J. G., F. P. R. Verbeek, B. E. Schaafsma, M. C. Boonstra, J. R. van der Vorst, G.-J. Liefers, C. J. H. van de Velde, J. V. Frangioni and A. L. Vahrmeijer (2014) Real-time intraoperative detection of breast cancer using near-infrared fluorescence imaging and methylene blue. *Eur J Surg Oncol* **40**(7), 850–858. https://doi.org/10.1016/j.ejso.2014.02.225
8. Shin, D., M. C. Pierce, A. M. Gillenwater, M. D. Williams and R. R. Richards-Kortum (2010) A fiber-optic fluorescence microscope using a consumer-grade digital camera for in vivo cellular imaging. *PLoS One* **5**(6), e11218. https://doi.org/10.1371/journal.pone.0011218
9. Pathak, I., N. L. Davis, Y. N. Hsiang, N. F. Quenville and B. Palcic (1995) Detection of squamous neoplasia by fluorescence imaging comparing porfimer sodium fluorescence to tissue autofluorescence in the hamster cheek-pouch model. *Am. J. Surg.* **170**(5), 423–426. https://doi.org/10.1016/S0002-9610(99)80321-3
10. Sachar, M., K. E. Anderson and X. Ma (2016) Protoporphyrin IX: The good, the bad, and the ugly. *J. Pharmacol. Exp. Therap.* **356**(2), 267–275. https://doi.org/10.1124/jpet.115.228130
11. Hadjipanayis, C. G., G. Widhalm and W. Stummer (2015) What is the surgical benefit of utilizing 5-aminolevulinic acid for fluorescence-guided surgery of malignant gliomas? *Neurosurgery* **77**(5), 663–673. https://doi.org/10.1227/NEU.0000000000000929 [in Eng].
12. Stummer, W., U. Pichlmeier, T. Meinel, O. D. Wiestler, F. Zanella and H.-J. Reulen (2006) Fluorescence-guided surgery with 5-aminolevulinic acid for resection of malignant glioma: A randomised controlled multicentre phase III trial. *Lancet Oncol.* **7**(5), 392–401. https://doi.org/10.1016/s1470-2045(06)70665-9
13. Holliger, P. and P. J. Hudson (2005) Engineered antibody fragments and the rise of single domains. *Nat. Biotechnol.* **23**(9), 1126–1136. https://doi.org/10.1038/nbt1142
14. van Dam, G., G. Themelis, L. Crane, N. Harlaar, R. Pleijhuis, W. Kelder, A. Sarantopoulos, J. de Jong, H. Arts, A. van der Zee, J. Bart, P. Low and V. Ntziachristos (2011) Intraoperative tumor-specific fluorescence imaging in ovarian cancer by folate receptor-α targeting: first in-human results. *Nat. Med.* **17**(10), 1315–1319. https://doi.org/10.1038/nm.2472
15. Manning, C., N. Merchant, A. Foutch, J. Virostko, S. Wyatt, C. Shah, E. McKinley, J. Xie, N. Mutic, M. Washington, B. LaFleur, M. Tantawy, T. Peterson, M. Ansari, R. Baldwin, M. Rothenberg, D. Bornhop, J. Gore and R. Coffey (2008) Molecular Imaging of Therapeutic Response to Epidermal Growth Factor Receptor Blockade in Colorectal Cancer. *Clin. Cancer Res.* **14**(22), 7413–7422. https://doi.org/10.1158/1078-0432.ccr-08-0239
16. Beilke, L. D., L. M. Aleksunes, E. R. Olson, D. G. Besselsen, C. D. Klaassen, K. Dvorak and N. J. Cherrington (2009) Decreased apoptosis during CAR-mediated hepatoprotection against lithocholic acid-induced liver injury in mice. *Toxicol. Lett.* **188**(1), 38–44. https://doi.org/10.1016/j.toxlet.2009.03.005
17. Pogue, B., K. Samkoe, S. Hextrum, J. O'Hara, M. Jermyn, S. Srinivasan and T. Hasan (2010) Imaging targeted-agent binding in vivo with two probes. *J. Biomed. Opt.* **15**(3), 030513. https://doi.org/10.1117/1.3449109
18. Lin, X., H. Zhu, Z. Luo, Y. Hong, H. Zhang, X. Liu, H. Ding, H. Tian and Z. Yang (2014) Near-infrared fluorescence imaging of non-Hodgkin's lymphoma CD20 expression using Cy7-conjugated Obinutuzumab. *Mol. Imaging Biol.* **16**(6), 877–887. https://doi.org/10.1007/s11307-014-0742-3
19. Ballou, B., G. Fisher, A. Waggoner, D. Farkas, J. Reiland, R. Jaffe, R. Mujumda, S. Mujumdar and T. Hakala (1995) Tumor labeling in vivo using cyanine-conjugated monoclonal antibodies. *Cancer Immunol Immunother* **41**(4), 257–263. https://doi.org/10.1007/bf01517001
20. Kim, K., H. Park and K. M. Lim (2015) Phototoxicity: Its mechanism and animal alternative test methods. *Toxicol. Res.* **31**(2), 97–104. https://doi.org/10.5487/TR.2015.31.2.097
21. Huang, L., Y. Xuan, Y. Koide, T. Zhiyentayev, M. Tanaka and M. R. Hamblin (2012) Type I and type II mechanisms of antimicrobial photodynamic therapy: An in vitro study on gram-negative and gram-positive bacteria. *Lasers Surg. Med.* **44**(6), 490–499. https://doi.org/10.1002/lsm.22045 [in Eng].
22. Garcia-Diaz, M., Y.-Y. Huang and M. R. Hamblin (2016) Use of fluorescent probes for ROS to tease apart type I and type II photochemical pathways in photodynamic therapy. *Methods* **109**, 158–166. https://doi.org/10.1016/j.ymeth.2016.06.025 [in Eng].
23. Stadtman, E. R. and R. L. Levine (2006) Protein oxidation. *Ann. N. Y. Acad. Sci.* **899**(1), 191–208. https://doi.org/10.1111/j.1749-6632.2000.tb06187.x
24. Fruhwirth, G. O. and A. Hermetter (2008) Mediation of Apoptosis by Oxidized Phospholipids. *Lipids in Health and Disease*, pp. 351–367. Springer, Dordrecht, Netherlands.
25. Auten, R. L., M. H. Whorton and S. Nicholas Mason (2002) Blocking neutrophil influx reduces DNA damage in hyperoxia-exposed newborn rat lung. *Am. J. Respir. Cell Mol. Biol.* **26**(4), 391–397. https://doi.org/10.1165/ajrcmb.26.4.4708
26. Foote, C. S. (1968) Mechanisms of photosensitized oxidation. *Science* **162**(3857), 963–970. https://doi.org/10.1126/science.162.3857.963
27. *Singlet Oxygen* (Comprehensive Series in Photochemical & Photobiological Sciences). 2016.
28. Lin, H., Y. Shen, D. Chen, L. Lin, B. Wilson, B. Li and S. Xie (2013) Feasibility study on quantitative measurements of singlet oxygen generation using singlet oxygen sensor green. *J. Fluoresc.* **23**(1), 41–47. https://doi.org/10.1007/s10895-012-1114-5
29. Lutkus, L. V., S. S. Rickenbach and T. M. McCormick (2019) Singlet oxygen quantum yields determined by oxygen consumption. *J. Photochem. Photobiol. A Chem.* **378**, 131–135. https://doi.org/10.1016/j.jphotochem.2019.04.029
30. Kennedy, J. C., R. H. Pottier and D. C. Pross (1990) Photodynamic therapy with endogenous protoporphyrin: IX: Basic principles and present clinical experience. *J. Photochem. Photobiol. B Biol.* **6**(1), 143–148. https://doi.org/10.1016/1011-1344(90)85083-9
31. Stepp, H. and W. Stummer (2018) 5-ALA in the management of malignant glioma. *Lasers Surg. Med.* **50**(5), 399–419. https://doi.org/10.1002/lsm.22933
32. Nishimura, T., M. Mitsunaga, R. Sawada, M. Saruta, H. Kobayashi, N. Matsumoto, T. Kanke, H. Yanai and K. Nakamura (2019) Photoimmunotherapy targeting biliary-pancreatic cancer with humanized anti-TROP2 antibody. *Cancer Med.* **8**(18), 7781–7792. https://doi.org/10.1002/cam4.2658 [in Eng].
33. Isobe, Y., et al. (2020) Near infrared photoimmunotherapy targeting DLL3 for small cell lung cancer. *EBioMedicine* **52**, 102632. https://doi.org/10.1016/j.ebiom.2020.102632 [in Eng].
34. Nagaya, T., K. Sato, T. Harada, Y. Nakamura, P. L. Choyke and H. Kobayashi (2015) Near infrared photoimmunotherapy targeting EGFR positive triple negative breast cancer: Optimizing the conjugate-light regimen. *PLoS One* **10**(8), e0136829. https://doi.org/10.1371/journal.pone.0136829 [in Eng].
35. McBride, T. J., J. E. Schneider, R. A. Floyd and L. A. Loeb (1992) Mutations induced by methylene blue plus light in single-stranded

M13mp2. *Proc. Natl. Acad. Sci. USA* **89**(15), 6866–6870. https://doi.org/10.1073/pnas.89.15.6866 [in Eng].
36. Olliver, C., Jr., P. Wild, S. D. Sahay and L. Hardie (2003) Chromoendoscopy with methylene blue and associated DNA damage in Barrett's oesophagus. *Lancet* **362**(9381), 373–374. https://doi.org/10.1016/s0140-6736(03)14026-3
37. Lytle, C. D., P. G. Carney, R. P. Felten, H. F. Bushar and R. C. Straight (1989) Inactivation and mutagenesis of herpes virus by photodynamic treatment with therapeutic dyes. *Photochem. Photobiol.* **50**(3), 367–371. https://doi.org/10.1111/j.1751-1097.1989.tb04171.x [in Eng].
38. Ravanat, J. L., S. Sauvaigo, S. Caillat, G. R. Martinez, M. H. Medeiros, P. Di Mascio, A. Favier and J. Cadet (2004) Singlet oxygen-mediated damage to cellular DNA determined by the comet assay associated with DNA repair enzymes. *Biol. Chem.* **385**(1), 17–20. https://doi.org/10.1515/BC.2004.003
39. Tummers, W. S., J. Warram, K. Tipirneni, J. Fengler, P. Jacobs, L. Shankar, L. Henderson, B. Ballard, J. Pfefer, B. W. Pogue, J. P. Weichert, M. Bouvet, J. Sorger, C. H. Contag, J. V. Frangioni, M. F. Tweedle, J. P. Basilion, S. Gambhir and E. Rosenthal (2017) Regulatory aspects of optical methods and exogenous targets for cancer detection. *Cancer Res.* **77**(9), 2197–2206. https://doi.org/10.1158/0008-5472.Can-16-3217
40. Kim, S., M. Fujitsuka and T. Majima (2013) Photochemistry of singlet oxygen sensor green. *J. Phys. Chem. B.* **117**(45), 13985–13992. https://doi.org/10.1021/jp406638g
41. Prasad, A., M. Sedlářová and P. Pospíšil (2018) Singlet oxygen imaging using fluorescent probe Singlet Oxygen Sensor Green in photosynthetic organisms. *Sci. Rep.* **8**(1), 1–13. https://doi.org/10.1038/s41598-018-31638-5
42. Obaid, G., W. Jin, S. Bano, D. Kessel and T. Hasan (2019) Nanolipid formulations of benzoporphyrin derivative: Exploring the dependence of Nanoconstruct Photophysics and photochemistry on their therapeutic index in ovarian cancer cells. *Photochem. Photobiol.* **95**(1), 364–377. https://doi.org/10.1111/php.13002
43. Flors, C., M. J. Fryer, J. Waring, B. Reeder, U. Bechtold, P. M. Mullineaux, S. Nonell, M. T. Wilson and N. R. Baker (2006) Imaging the production of singlet oxygen in vivo using a new fluorescent sensor, singlet oxygen sensor green. *J. Exp. Bot.* **57**(8), 1725–1734. https://doi.org/10.1093/jxb/erj181
44. Inglut, C. T., B. Gaitan, D. Najafali, I. A. Lopez, N. P. Connolly, S. Orsila, R. Perttilä, G. F. Woodworth, Y. Chen and H. C. Huang (2020) Predictors and limitations of the penetration depth of photodynamic effects in the rodent brain. *Photochem. Photobiol.* **96**(2), 301–309. https://doi.org/10.1111/php.13155 [in Eng].
45. Tanaka, K., T. Miura, N. Umezawa, Y. Urano, K. Kikuchi, T. Higuchi and T. Nagano (2001) Rational design of fluorescein-based fluorescence probes. Mechanism-based design of a maximum fluorescence probe for singlet oxygen. *J. Am. Chem. Soc.* **123**(11), 2530–2536. https://doi.org/10.1021/ja0035708
46. Arora, R., M. Ridha, D. Lee, J. Elliott, H. Rosenberg, M. Diop, T. Y. Lee and K. St. Lawrence (2013) Preservation of the metabolic rate of oxygen in preterm infants during indomethacin therapy for closure of the ductus arteriosus. *Pediatr. Res.* **73**(6), 713–718. https://doi.org/10.1038/pr.2013.53
47. IC-GREEN® (indocyanine green for injection USP) For Intravenous Injection. https://www.accessdata.fda.gov/drugsatfda_docs/label/2006/011525s017lbl.pdf (accessed August 2020).
48. Zhu, B. and E. M. Sevick-Muraca (2015) A review of performance of near-infrared fluorescence imaging devices used in clinical studies. *Br. J. Radiol.* **88**(1045), 20140547. https://doi.org/10.1259/bjr.20140547
49. Peter, C., D. Hongwan, A. Küpfer and B. H. Lauterburg (2000) Pharmacokinetics and organ distribution of intravenous and oral methylene blue. *Eur. J. Clin. Pharmacol.* **56**(3), 247–250. https://doi.org/10.1007/s002280000124
50. Matsui, A., E. Tanaka, H. S. Choi, V. Kianzad, S. Gioux, S. I. Lomnes and J. V. Frangioni (2010) Real-time, near-infrared, fluorescence-guided identification of the ureters using methylene blue. *Surgery* **148**(1), 78–86. https://doi.org/10.1016/j.surg.2009.12.003
51. Gao, R. W., N. Teraphongphom, E. de Boer, N. S. van den Berg, V. Divi, M. J. Kaplan, N. J. Oberhelman, S. S. Hong, E. Capes, A. D. Colevas, J. M. Warram and E. L. Rosenthal (2018) Safety of panitumumab-IRDye800CW and cetuximab-IRDye800CW for fluorescence-guided surgical navigation in head and neck cancers. *Theranostics* **8**(9), 2488–2495. https://doi.org/10.7150/thno.24487 [in Eng].
52. Miller, S. E., W. S. Tummers, N. Teraphongphom, N. S. van Den Berg, A. Hasan, R. D. Ertsey, S. Nagpal, L. D. Recht, E. D. Plowey, H. Vogel, G. R. Harsh, G. A. Grant, G. H. Li and E. Rosenthal (2018) First-in-human intraoperative near-infrared fluorescence imaging of glioblastoma using cetuximab-IRDye800. *J. Neurooncol* **139**(1), 135–143. https://doi.org/10.1007/s11060-018-2854-0
53. Ito, K., M. Mitsunaga, T. Nishimura, H. Kobayashi and H. Tajiri (2016) Combination photoimmunotherapy with monoclonal antibodies recognizing different epitopes of human epidermal growth factor receptor 2: An assessment of phototherapeutic effect based on fluorescence molecular imaging. *Oncotarget* **7**(12), 14143–14152. https://doi.org/10.18632/oncotarget.7490
54. De Boer, E., S. Samuel, D. N. French, J. M. Warram, T. R. Schoeb, E. L. Rosenthal and K. R. Zinn (2016) Biodistribution study of intravenously injected cetuximab-IRDye700DX in cynomolgus macaques. *Mol. Imaging Biol.* **18**(2), 232–242. https://doi.org/10.1007/s11307-015-0892-y
55. Dsouza, A. V., H. Lin, E. R. Henderson, K. S. Samkoe and B. W. Pogue (2016) Review of fluorescence guided surgery systems: Identification of key performance capabilities beyond indocyanine green imaging. *J. Biomed. Opt.* **21**(8), 080901. https://doi.org/10.1117/1.jbo.21.8.080901
56. Tang, Y., J. Carns, A. D. Polydorides, S. Anandasabapathy and R. R. Richards-Kortum (2016) In vivowhite light and contrast-enhanced vital-dye fluorescence imaging of Barrett's-related neoplasia in a single-endoscopic insertion. *J. Biomed. Opt.* **21**(8), 086004. https://doi.org/10.1117/1.jbo.21.8.086004
57. Pérez-Laguna, V., I. García-Luque, S. Ballesta, L. Pérez-Artiaga, V. Lampaya-Pérez, S. Samper, P. Soria-Lozano, A. Rezusta and Y. Gilaberte (2018) Antimicrobial photodynamic activity of rose Bengal, alone or in combination with gentamicin, against planktonic and biofilm Staphylococcus aureus. *Photodiagnosis Photodyn. Ther.* **21**, 211–216. https://doi.org/10.1016/j.pdpdt.2017.11.012
58. Tanielian, C. and G. Heinrich (1995) Effect of aggregation on the hematoporphyrin-sensitized production of singlet molecular oxygen. *Photochem. Photobiol.* **61**(2), 131–135. https://doi.org/10.1111/j.1751-1097.1995.tb03950.x
59. Mathai, S., T. A. Smith and K. P. Ghiggino (2007) Singlet oxygen quantum yields of potential porphyrin-based photosensitisers for photodynamic therapy. *Photochem. Photobiol. Sci.* **6**(9), 995. https://doi.org/10.1039/b705853e
60. Kiesslich, R., J. Fritsch, M. Holtmann, H. Koehler, M. Stolte, S. Kanzler, B. Nafe, M. Jung, P. R. Galle and M. F. Neurath (2003) Methylene blue-aided chromoendoscopy for the detection of intraepithelial neoplasia and colon cancer in ulcerative colitis. *Gastroenterology* **124**(4), 880–888. https://doi.org/10.1053/gast.2003.50146
61. Harrison, B. J. and F. Triponez (2009) Intraoperative adjuncts in surgery for primary hyperparathyroidism. *Langenbecks Arch. Surg.* **394**(5), 799–809. https://doi.org/10.1007/s00423-009-0532-6
62. Winer, J. H., H. S. Choi, S. L. Gibbs-Strauss, Y. Ashitate, Y. L. Colson and J. V. Frangioni (2010) Intraoperative localization of insulinoma and normal pancreas using invisible near-infrared fluorescent light. *Ann. Surg. Oncol.* **17**(4), 1094–1100. https://doi.org/10.1245/s10434-009-0868-8
63. Kluk, J., R. Charles-Holmes and D. Markham (2012) Acute phototoxicity induced by methylene blue-assisted parathyroidectomy: An unreported risk of a common procedure. *Br. J. Dermatol.* **166**(4), 907–908. https://doi.org/10.1111/j.1365-2133.2011.10703.x
64. Sills, M. R. and W. H. Zinkham (1994) Methylene blue-induced Heinz body hemolytic anemia. *Arch. Pediatr. Adolesc. Med.* **148**(3), 306–310. https://doi.org/10.1001/archpedi.1994.02170030076017 [in Eng].
65. Porat, R., S. Gilbert and D. Magilner (1996) Methylene blue-induced phototoxicity: An unrecognized complication. *Pediatrics* **97**(5), 717–721 [in Eng].
66. Davies, J., D. Burke, J. R. Olliver, L. J. Hardie, C. P. Wild and M. N. Routledge (2007) Methylene blue but not indigo carmine causes DNA damage to colonocytes in vitro and in vivo at concentrations used in clinical chromoendoscopy. *Gut* **56**(1), 155–156. https://doi.org/10.1136/gut.2006.107300

67. C. M. Klais, M. D. Ober and L. A. Yannuzzi (2009) Indocyanine green angiography: General aspects and interpretation. In *Retinal Angiography and Optical Coherence Tomography*, Chapter 3, (Edited by F. Arevalo), pp. 43–59. Springer New York
68. Balamurugan, S., A. Agrawal, Y. Kato and H. Sano (2011) Intra operative indocyanine green video-angiography in cerebrovascular surgery: An overview with review of literature. *Asian J. Neurosurg.* **6**(2), 88–93. https://doi.org/10.4103/1793-5482.92168 [in Eng].
69. Unno, N., K. Inuzuka, M. Suzuki, N. Yamamoto, D. Sagara, M. Nishiyama and H. Konno (2007) Preliminary experience with a novel fluorescence lymphography using indocyanine green in patients with secondary lymphedema. *J. Vasc. Surg*. **45**(5), 1016–1021. https://doi.org/10.1016/j.jvs.2007.01.023
70. Lee, J. Y. K., J. T. Pierce, R. Zeh, S. S. Cho, R. Salinas and S. Nie (2017) Intraoperative near-infrared optical contrast can localize brain metastases. *World Neurosurg*. **106**, 120–130. https://doi.org/10.1016/j.wneu.2017.06.128
71. Chen, Q. Y., J. W. Xie, Q. Zhong, J. B. Wang, J. X. Lin, J. Lu, L. L. Cao., M. Lin, R. H. Tu, Z. N. Huang, J. H. Lin, H. L. Zheng, P. Li, C. H. Zheng and C. M. Huang (2020) Safety and efficacy of indocyanine green tracer-guided lymph node dissection during laparoscopic radical gastrectomy in patients with gastric cancer. *JAMA Surg*. **155**(4), 300. https://doi.org/10.1001/jamasurg.2019.6033
72. Engel, E., R. D. Schraml, T. Maisch, K. Kobuch, B. König, R. M. Szeimies, J. Hillenkamp, W. Bäumler and R. Vasold (2008) Light-induced decomposition of indocyanine green. *Invest. Opthalmol. Vis. Sci.* **49**(5), 1777. https://doi.org/10.1167/iovs.07-0911
73. Dimofte, A., J. C. Finlay and T. C. Zhu (2005) A method for determination of the absorption and scattering properties interstitially in turbid media. *Phys. Med. Biol.* **50**(10), 2291–2311. https://doi.org/10.1088/0031-9155/50/10/008
74. Jacques, S. L. (2010) How tissue optics affect dosimetry of photodynamic therapy. *J. Biomed. Opt.* **15**(5), 051608. https://doi.org/10.1117/1.3494561
75. Takeuchi, M., T. Sugie, K. Abdelazeem, H. Kato, N. Shinkura, M. Takada, H. Yamashiro, T. Ueno and M. Toi (2012) Lymphatic mapping with fluorescence navigation using indocyanine green and axillary surgery in patients with primary breast cancer. *Breast J.* **18**(6), 535–541. https://doi.org/10.1111/tbj.12004
76. Imai, T., K. Takahashi, F. Goto and Y. Morishita (1998) Measurement of blood concentration of indocyanine green by pulse dye densitometry – Comparison with the conventional spectrophotometric method. *J. Clin. Monit. Comput.* **14**(7–8), 477–484. https://doi.org/10.1023/a:1009948128543
77. Tagaya, N., R. Yamazaki, A. Nakagawa, A. Abe, K. Hamada, K. Kubota and T. Oyama (2008) Intraoperative identification of sentinel lymph nodes by near-infrared fluorescence imaging in patients with breast cancer. *Am. J. Surg*. **195**(6), 850–853. https://doi.org/10.1016/j.amjsurg.2007.02.032
78. Di Stefano, A. F. D., M. M. Radicioni, A. Vaccani, A. Fransioli, L. Longo, L. Moro and A. Repici (2018) Methylene blue MMX® tablets for chromoendoscopy. Bioavailability, colon staining and safety in healthy volunteers undergoing a full colonoscopy. *Contemp. Clin. Trials* **71**, 96–102. https://doi.org/10.1016/j.cct.2018.06.001
79. Sato, K., R. Watanabe, H. Hanaoka, T. Harada, T. Nakajima, I. Kim, C. H. Paik, P. L. Choyke and H. Kobayashi (2014) Photoimmunotherapy: Comparative effectiveness of two monoclonal antibodies targeting the epidermal growth factor receptor. *Mol. Oncol.* **8**(3), 620–632. https://doi.org/10.1016/j.molonc.2014.01.006
80. Wilkinson, F., W. P. Helman and A. B. Ross (1993) Quantum yields for the photosensitized formation of the lowest electronically excited singlet state of molecular oxygen in solution. *J. Phys. Chem. Ref. Data Monogr.* **22**(1), 113–262. https://doi.org/10.1063/1.555934
81. Kishimoto, S., M. Bernardo, K. Saito, S. Koyasu, J. B. Mitchell, P. L. Choyke and M. C. Krishna (2015) Evaluation of oxygen dependence on in vitro and in vivo cytotoxicity of photoimmunotherapy using IR-700–antibody conjugates. *Free Radic. Biol. Med.* **85**, 24–32. https://doi.org/10.1016/j.freeradbiomed.2015.03.038